Supplementary Materials for

Giant longitudinal and transverse magneto thermoelectric effects in a van del Waals semimetal $TaCo_2Te_2$

Zhigang Gui[1], Ye Yang[1], Xikai Wen[1], Yuqing Zhang[1], Yikang Li[1], Yanjun Li[1], Qingyuan Liu[1], Mingjie Wang[3], Jianjun Ying[1,2†], and Xianhui Chen[1,2,4†]

[1]Department of Physics, and CAS Key Laboratory of Strongly-coupled Quantum Matter Physics, University of Science and Technology of China, Hefei, Anhui 230026, China

[2]Hefei National Laboratory, Hefei 230088, China

[3]School of Physics and Optoelectronic Engineering, Anhui University, Hefei, Anhui230601, China

[4]Collaborative Innovation Center of Advanced Microstructures, Nanjing University, Nanjing, 210093, China

*Correspondence to: yingjj@ustc.edu.cn, chenxh@ustc.edu.cn

MATERIALS AND METHODS

Sample preparation

Single crystals of $TaCo_2Te_2$ were synthesized by chemical vapor transport using iodine as a transport agent[1, 2]. Ta powder, Co powder and Te ingot were mixed in a certain molar ratio[1, 2] and sealed in a quartz tube under high vacuum. The tube was placed in a horizontal gradient furnace. The power side (hot side) was heated to 1173 K, while the other side (cold side) was heated to 1073 K and maintained for two weeks.

Sample Characterization

X-ray diffraction data were collected at room temperature using an X-ray diffractometer (SmartLab-9, Rikagu) with Cu K_α radiation and a fixed graphite monochromator. The thermopower and kappa were measured with a home-built setup by applying an alternating heat current through the sample (AC method) in a 14T-TeslaTron-PT system (Oxford Instrument). Resistivity and Hall resistivity were measured on the same sample using the standard four-probe method in a PPMS-14T system (Quantum Design).

Calculation Method

The Vienna ab initio simulation package (VASP)[3] can be employed to calculate the electronic structure. The Perdew–Burke–Ernzerhof (PBE) functional[4] describes the exchange correlation energy. The cutoff energy of the plane-wave basis was set to 500 eV. The sampled kmesh consists of 8 × 8 × 3 Monkhorst-Pack grids for structural optimization. In addition, we adopt the VASPKIT[5] and FermiSurfer[6] codes to show the

Fermi surface.

Measurement setup

As depicted in the brief illustration of Fig. S3, the heater is meticulously attached to the sample using a high-quality thermal conductive adhesive, ensuring an efficient thermal connection. The temperature gradient is monitored through a differential thermocouple assembly, which comprises two thermocouples. To prevent the introduction of any additional thermoelectric potential, the electrodes for voltage measurement are crafted from gold. On the opposite side of the sample, a sapphire heat sink is connected, which serves to guarantee optimal heat conduction. This integrated assembly, consisting of the heater, sample, and heat sink, is securely mounted onto a base constructed from oxygen-free copper, again using thermal conductive adhesive. During the measurement process, the entire setup is enclosed within a sleeve that maintains a high vacuum condition of approximately 10^{-6} Pa.

Two-band model of the thermopower

When an external electrical field $\boldsymbol{E}$ is applied and a temperature gradient ∇T forms, the vector composed of the charge current $\boldsymbol{J}_{\mathrm{e}}$ and thermal current $\boldsymbol{J}_{\mathrm{heat}}$ can be expressed[7, 8] as

$$\begin{bmatrix} \boldsymbol{J}_{\mathrm{e}} \\ \boldsymbol{J}_{\mathrm{heat}} \end{bmatrix} = \begin{bmatrix} \boldsymbol{\sigma} & \boldsymbol{\alpha} \\ \boldsymbol{\alpha} T & \boldsymbol{\kappa} \end{bmatrix} \begin{bmatrix} \boldsymbol{E} \\ -\nabla T \end{bmatrix} \tag{S1}$$

where $\boldsymbol{\sigma}$, $\boldsymbol{\alpha}$, and $\boldsymbol{\kappa}$ represent the electrical conductivity tensor, thermoelectrical conductivity tensors and thermal conductivity tensor, respectively. Therefore, the electrical current can be expressed as

$$\boldsymbol{J}_{\mathrm{e}} = \boldsymbol{\sigma} \cdot \boldsymbol{E} - \boldsymbol{\alpha} \cdot (\nabla T) \tag{S2}$$

In our work, only heat is supplied by the heater without an extra current applied in the TE measurement, demonstrating that $\boldsymbol{J}_{\mathrm{e}}$ is zero. Considering 2D conditions, i.e., the electrical conductivity tensor has only in-plane components σ_{xx}, σ_{xy}, σ_{yy}, σ_{yx}, and electrical field only has two components of E_x and E_y. Therefore, equation S2 can be expressed as

$$\begin{bmatrix} \sigma_{xx} & \sigma_{xy} \\ \sigma_{yx} & \sigma_{yy} \end{bmatrix} \begin{bmatrix} E_x \\ E_y \end{bmatrix} = \begin{bmatrix} \alpha_{xx} & \alpha_{xy} \\ \alpha_{yx} & \alpha_{yy} \end{bmatrix} \begin{bmatrix} \nabla_x T \\ \nabla_y T \end{bmatrix} \tag{S3}$$

Since the temperature gradient $\nabla \boldsymbol{T}$ is only along the longitudinal direction, $\nabla_y T$ is zero. Based on Onsager's relation[9], $\sigma_{xy} = -\sigma_{yx}$ and $\alpha_{xy} = -\alpha_{yx}$, equation S3 can be simplified as

$$\begin{bmatrix} E_x \\ E_y \end{bmatrix} = \begin{bmatrix} \sigma_{xx} & \sigma_{xy} \\ \sigma_{yx} & \sigma_{yy} \end{bmatrix}^{-1} \begin{bmatrix} \alpha_{xx} \\ \alpha_{yx} \end{bmatrix} \nabla_x T = \frac{1}{\sigma_{xx}\sigma_{yy} + \sigma_{xy}^2} \begin{bmatrix} \sigma_{yy}\alpha_{xx} + \sigma_{yx}\alpha_{yx} \\ \sigma_{xx}\alpha_{yx} - \sigma_{yx}\alpha_{xx} \end{bmatrix} \nabla_x T \tag{S4}$$

Combined with the definition of the thermopower $S = -\dfrac{\boldsymbol{E}}{\nabla T}$, the corresponding longitudinal and transverse thermopowers can be obtained as

$$S_{xx} = -\frac{E_x}{\nabla_x T} = -\frac{\sigma_{xx}\alpha_{xx} + \sigma_{yx}\alpha_{yx}}{\sigma_{xx}\sigma_{yy} + \sigma_{xy}^2} \tag{S5}$$

$$S_{xy} = -\frac{E_y}{\nabla_y T} = -\frac{\sigma_{xx}\alpha_{yx} - \sigma_{yx}\alpha_{xx}}{\sigma_{xx}\sigma_{yy} + \sigma_{xy}^2} \tag{S6}$$

Considering two carriers, electrons and holes, in our work, the electrical conductivity and thermoelectrical conductivity can be expressed as

$$\sigma_{xx} = \sigma_{xx}^e + \sigma_{xx}^h \tag{S7}$$

$$\sigma_{yx} = \sigma_{yx}^e + \sigma_{yx}^h \tag{S8}$$

$$\alpha_{xx} = \alpha_{xx}^e + \alpha_{xx}^h \tag{S9}$$

$$\alpha_{yx} = \alpha_{yx}^e + \alpha_{yx}^h \tag{S10}$$

Therefore, neglecting the slight anisotropy in electrical resistivity, equations S5 and S6 can be rewritten as

$$S_{xx} = -\frac{[S_{xx}^e(\sigma_{xx}^e\sigma_{xx} + \sigma_{yx}^e\sigma_{yx}) + S_{xx}^h(\sigma_{xx}^h\sigma_{xx} + \sigma_{yx}^h\sigma_{yx}) + S_{yx}^e(\sigma_{xx}^e\sigma_{yx} - \sigma_{yx}^e\sigma_{yx}) + S_{yx}^h(\sigma_{xx}^h\sigma_{yx} - \sigma_{yx}^h\sigma_{xx})]}{\sigma_{xx}^2 + \sigma_{yx}^2} \tag{S11}$$

$$S_{xy} = \frac{[S_{xx}^e(\sigma_{yx}^e\sigma_{xx} - \sigma_{xx}^e\sigma_{yx}) + S_{xx}^h(\sigma_{xx}^h\sigma_{xx} - \sigma_{xx}^h\sigma_{yx}) + S_{yx}^e(\sigma_{xx}^e\sigma_{xx} + \sigma_{yx}^e\sigma_{yx}) + S_{yx}^h(\sigma_{yx}^h\sigma_{yx} + \sigma_{yx}^h\sigma_{yx})]}{\sigma_{xx}^2 + \sigma_{yx}^2} \tag{S12}$$

For the multiband model, under a perpendicular magnetic field, the carrier concentration and mobility can be acquired[10] by

$$\sigma_{xx}^i = \frac{n_i e\mu_i}{1 + \mu_i^2 B_z^2} \tag{S13}$$

$$\sigma_{xy}^{i} = \frac{n_i e\mu_i}{1+\mu_i^2 B_z^2}\mu_i B_z \tag{S14}$$

where n, e, μ, and B_z are the carrier concentration, electron charge, mobility and magnetic field, respectively. Here, i denotes the number of bands. In our two-carrier system, the signs of n and μ for electrons are negative, while they are positive for holes. Accordingly, n_i and μ_i can be fitted by equations S7, S8, S13 and S14.

By constant relaxation time approximation, equations (11) and (12) can be expressed as

$$S_{xx} = -\frac{S_{xx}^{e}(\sigma_{xx}^{e}\sigma_{xx} + \sigma_{yx}^{e}\sigma_{yx}) + S_{xx}^{h}(\sigma_{xx}^{h}\sigma_{xx} + \sigma_{yx}^{h}\sigma_{yx})}{\sigma_{xx}^{2}} \tag{S15}$$

$$S_{xy} = \frac{S_{xx}^{e}(\sigma_{yx}^{e}\sigma_{xx} - \sigma_{xx}^{e}\sigma_{yx}) + S_{xx}^{h}(\sigma_{yx}^{h}\sigma_{xx} - \sigma_{xx}^{h}\sigma_{yx})}{\sigma_{xx}^{2}} \tag{S16}$$

Further simplification for S_{xy} can be written as

$$S_{xy} = \frac{\sigma_{xx}^{e}\sigma_{xx}^{h}(\mu_e + \mu_h)B}{(\sigma_{xx}^{e} + \sigma_{xx}^{h})^2}(S_{xx}^{h} - S_{xx}^{e}) \tag{S17}$$

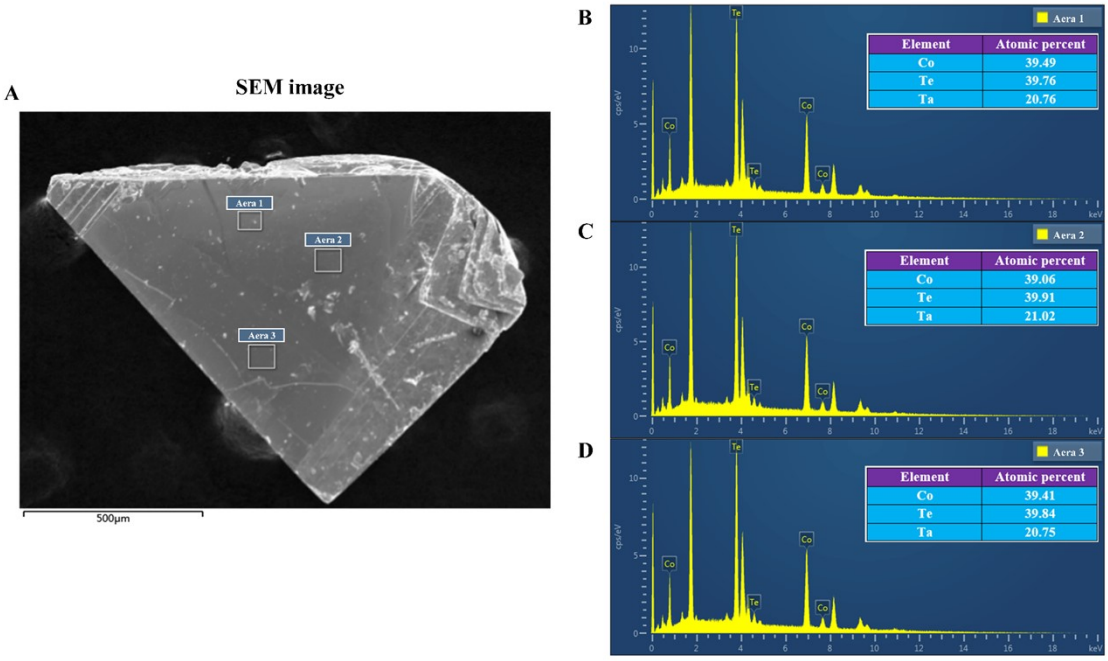

Fig. S1. Scanning electron microscopy (SEM) image and energy dispersive X-ray spectroscopy (EDS) of $TaCo_2Te_2$. (A) SEM image of a single crystal of $TaCo_2Te_2$. EDS spectra for (B)area 1, (C) aera 2 and (D) aera 3.

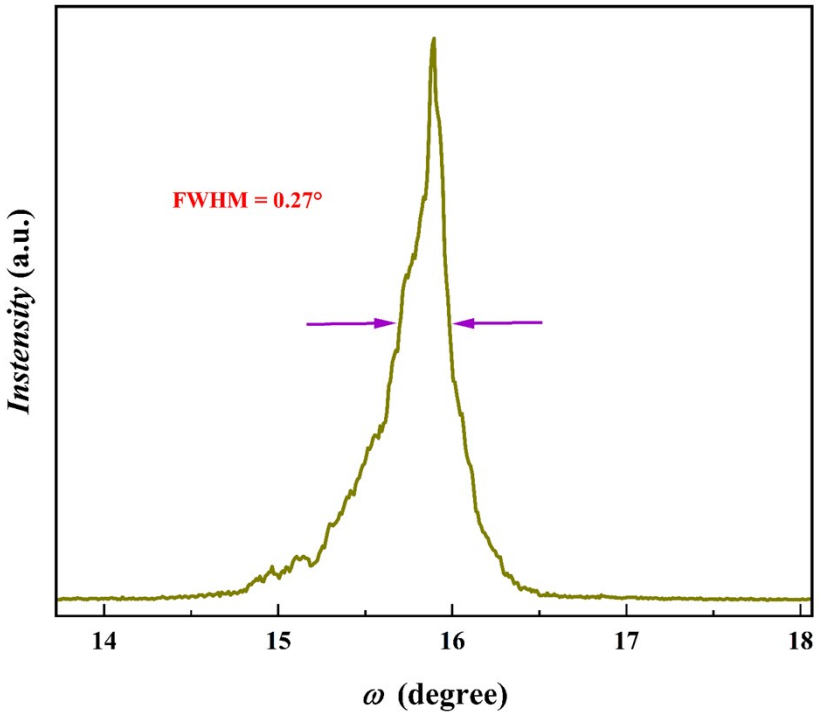

Fig. S2. Rocking curve of $TaCo_2Te_2$.

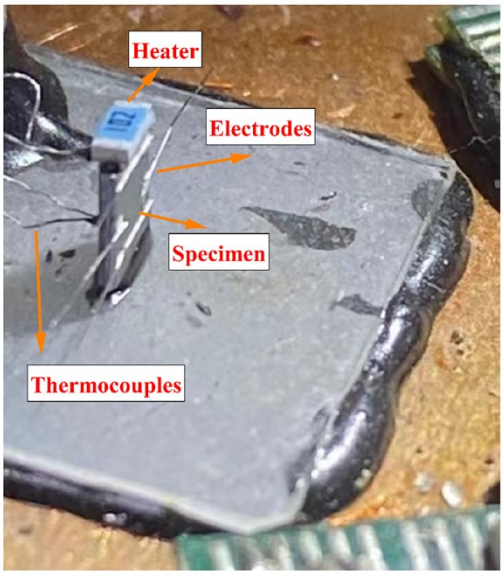

Fig. S3. Typical photograph for the sample mounting.

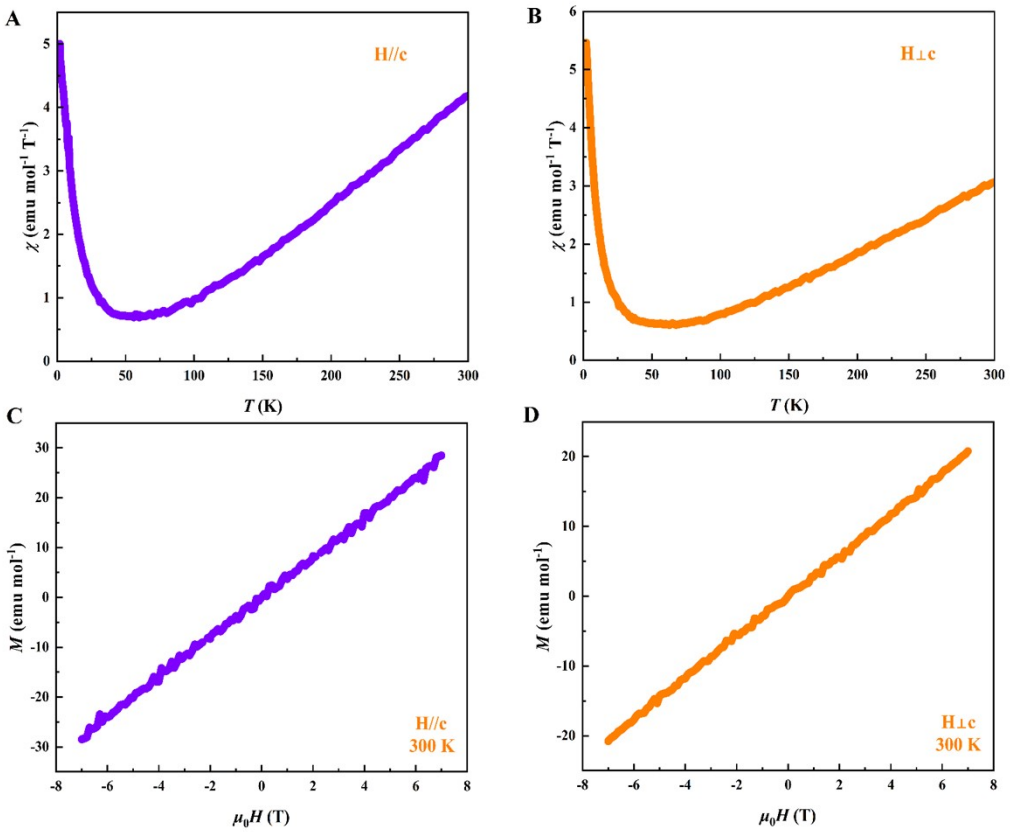

Fig. S4. Magnetization behaviors of $TaCo_2Te_2$ along different directions. (A) Temperature-dependent magnetic susceptibility along the direction (A) H//c and (B) H⊥c. Field-dependent magnetization along the direction (C) H//c and (D)H⊥c.

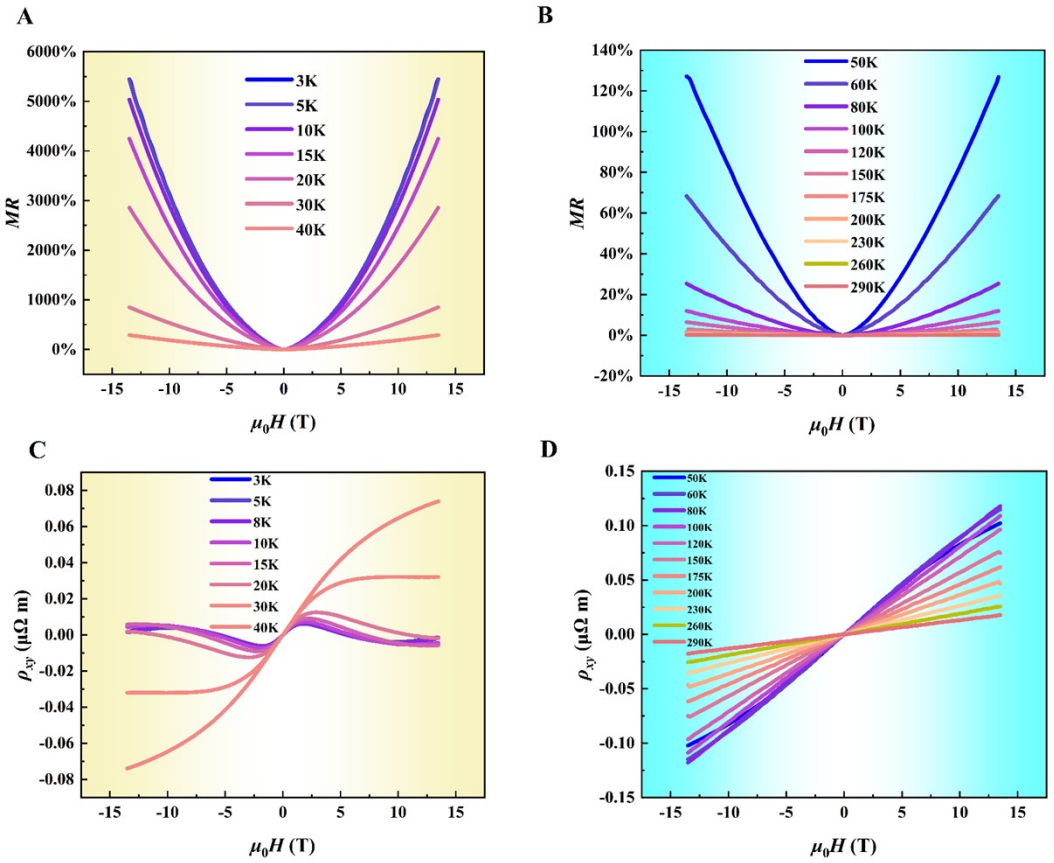

Fig. S5. Large magnetoresistance and Hall resistivity. Magnetoresistance of $TaCo_2Te_2$ from (A) 3-40K and (B) 50K-290K. Hall resistivity of $TaCo_2Te_2$ from (C) 3-40 K and (D) 50-290 K. In the electron-dominant region, $TaCo_2Te_2$ exhibits a large magnetoresistance of up to 5.5×10^3 % at 13.5 T, while the magnetoresistance is relatively low and decreases with increasing temperature in the hole-dominant region. The Hall resistivity of $TaCo_2Te_2$ shows anomalous behavior in the electron-dominant region but behaves linearly in the hole-dominant region.

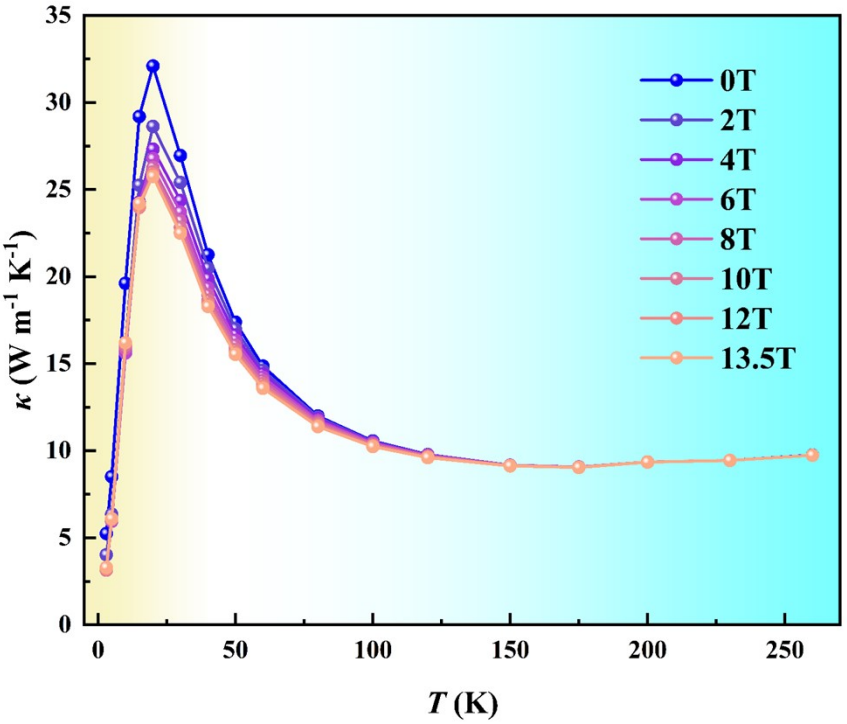

Fig. S6. Temperature-dependent thermal conductivity κ under different magnetic fields. Longitudinal thermal conductivity of $TaCo_2Te_2$ as a function of temperature measured at different magnetic fields. A slight suppression of κ under a magnetic field can be observed in the electron-dominant region, and the magnetic effect can be ignored with increasing temperature.

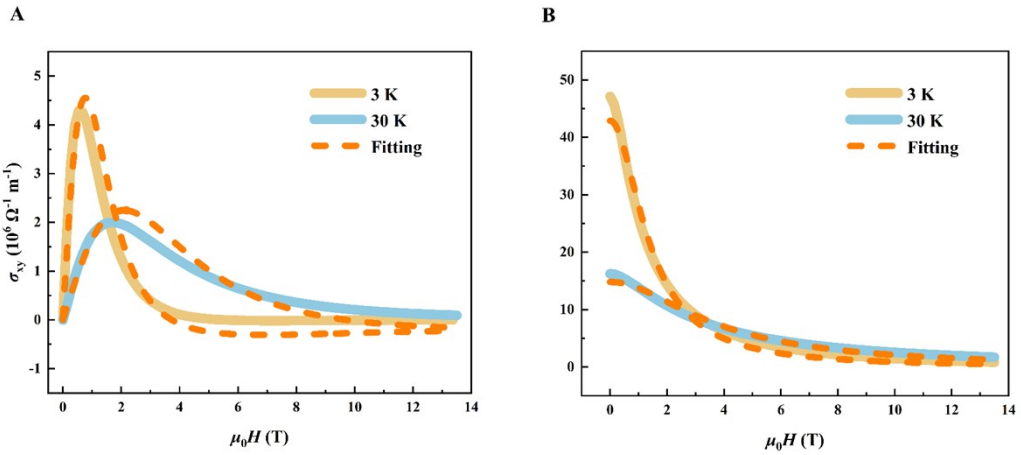

Fig. S7. Fitting results based on the two-band model. The (A) calculated Hall conductivity and (B) longitudinal conductivity with their fitting results at 3 K and 30 K.

Supplementary References

1. H. T. Rong, Z. Q. Huang, X. Zhang, S. Kumar, F. Y. Zhang, C. C. Zhang, Y. Wang, Z. Y. Hao, Y. Q. Cai, L. Wang, C. Liu, X. M. Ma, S. Guo, B. Shen, Y. Liu, S. T. Cui, K. Shimada, Q. S. Wu, J. H. Lin, Y. G. Yao, Z. W. Wang, H. Xu and C. Y. Chen, *Npj Quantum Materials*, 2023, **8**.
2. R. Singha, F. Yuan, G. M. Cheng, T. H. Salters, Y. M. Oey, G. V. Villalpando, M. Jovanovic, N. Yao and L. M. Schoop, *Adv. Funct. Mater.*, 2022, **32**, 9.
3. G. Kresse and J. Furthmuller, *Phys. Rev. B*, 1996, **54**, 11169-11186.
4. J. P. Perdew, K. Burke and M. Ernzerhof, *Phys. Rev. Lett.*, 1997, **78**, 1396-1396.
5. V. Wang, N. Xu, J. C. Liu, G. Tang and W. T. Geng, *Comput. Phys. Commun.*, 2021, **267**, 19.
6. M. Kawamura, *Comput. Phys. Commun.*, 2019, **239**, 197-203.
7. M. Ikhlas, T. Tomita, T. Koretsune, M. T. Suzuki, D. Nishio-Hamane, R. Arita, Y. Otani and S. Nakatsuji, *Nature Physics*, 2017, **13**, 1085-1090.
8. T. Miyasato, N. Abe, T. Fujii, A. Asamitsu, S. Onoda, Y. Onose, N. Nagaosa and Y. Tokura, *Phys. Rev. Lett.*, 2007, **99**, 4.
9. P. Jacquod, R. S. Whitney, J. Meair and M. Büttiker, *Phys. Rev. B*, 2012, **86**, 13.
10. B. S. Shastry, *Rep. Prog. Phys.*, 2009, **72**, 23.